Modelling mechanical behaviour of a gradient-microstructured material obtained by surface mechanical attrition treatment accounting for residual stresses

Zihao Guo, Jianqiang Zhou, Zhidan Sun, Delphine Retraint, Benoît Panicaud

To cite this version:

Zihao Guo, Jianqiang Zhou, Zhidan Sun, Delphine Retraint, Benoît Panicaud. Modelling mechanical behaviour of a gradient-microstructured material obtained by surface mechanical attrition treatment accounting for residual stresses. Mechanics of Materials, 2023, pp.104713. ⟨10.1016/j.mechmat.2023.104713⟩. ⟨hal-04121534⟩

Modelling mechanical behaviour of a gradient-microstructured material obtained by surface mechanical attrition treatment accounting for residual stresses

Zihao GUO[a], Jianqiang ZHOU[b], Zhidan SUN[a], Delphine RETRAINT[a] and Benoît PANICAUD[a, *]

[a] *LASMIS, Université de Technologie de Troyes (UTT), Troyes 10000, France*
[b] *School of Mechanical Engineering, Northwestern Polytechnical University, 710072, Xi'an, China*

ABSTRACT

In this work, an austenitic 316L steel was processed by surface mechanical attrition treatment (SMAT), and the induced gradient microstructure was highlighted by experimental measurements. A combined dislocation density-based and grain size-dependent constitutive model is developed to describe the mechanical behaviour of the gradient-microstructured material. In addition, this model also incorporates the grain size-dependent initial twin distribution and evolution of deformation twinning. Residual stress, initial dislocation density and twins are considered to reconstruct the depth-dependent residual fields induced by SMAT. Furthermore, the evolution of dislocation density and twin volume fraction is described during uniaxial tensile loading. Particular attention is devoted to investigate the effect of residual stress and deformation twinning on mechanical behaviour. Results of finite element simulation showed that the gradient microstructure enhances the yield strength, which is in agreement with previous experimental observations. It was revealed that residual stress significantly weakens the yield strength at the initial deformation stage, whereas it has little influence on the plastic behaviour at large deformation. The assumed grain size-dependent deformation twinning model allows describing the evolution of deformation twinning on gradient microstructure. The deformation twinning increases in relation to increased strain hardening during tensile loading. However, the evolution of twin volume fraction shows almost no twin and no variation of twinning within the nanocrystalline grain region.

Keywords: Gradient microstructure; Surface mechanical attrition treatment; Finite element analysis; Dislocation density-based constitutive model; Residual stress

1. Introduction

Gradient microstructure is usually introduced to optimize the surface conditions and mechanical properties of materials, which has shown a combination of high yield strength and good ductility as well as enhanced fatigue properties (Ao et al., 2019; Darling et al., 2016; Deng et al., 2016; Liu et al., 2013; Xiong et al., 2022). Gradient-

---

[*] Corresponding author.

E-mail address: benoit.panicaud@utt.fr (Benoît PANICAUD) microstructured materials (GMS) contain one or more gradient features (such as grain size, twin thickness, phase, chemical compound, etc.) along one specific direction, generally from the top surface to the bulk (Bahl et al., 2017; Liu et al., 2015; Wu et al., 2005; Lei et al., 2022). Recently, several approaches have been developed to form a gradient microstructure in metallic materials, including surface mechanical attrition treatment (SMAT) (An et al., 2013; Bahl et al., 2017), surface mechanical grinding treatment (SMGT) (Ghosh and Kain, 2010; Liu et al., 2015), ultrasonic surface rolling process (USRP) (Chen et al., 2022; Long et al., 2019), laser shock peening (LSP) (Maleki et al., 2022), etc.

Like similar mechanical surface treatment techniques, SMAT is able to generate a gradient microstructure with severe plastic deformation (SPD). The particularity of SMAT is that the gradient microstructure is generated by repeated random multi-directional impacts at a high strain rate on the surface layer of treated materials (Lu and Lu, 2004; Tao et al., 2002; Cai et al., 2015). During the SMAT process, a complex microstructure is induced due to the strain gradient distribution. A grain size distribution from a few nanometers to several microns is thus generated along the depth, from the top surface to the bulk of the SMATed samples (Lu and Lu, 2004; Tao et al., 2002). For some materials, SPD can also generate a gradient twinning region and/or martensite transformation, which could also significantly affect the mechanical behaviour of materials (Wu et al., 2005; Zhang et al., 2003; G.-H. Zhao et al., 2020; Zhu et al., 2004). Meanwhile, high compressive residual stresses are inevitably introduced into the near-surface region during the SMAT process, which can improve the fatigue features of materials (Dureau et al., 2022; Roland et al., 2006).

Many experimental characterizations have been carried out to reveal the mechanisms of GMS formation and evolution, especially by transmission electron microscopy (TEM) (Roland et al., 2007, 2006; Tao et al., 2002; Wen et al., 2009; Zhang et al., 2003; Zhu et al., 2004). It was found that grain refinement involves the onset of twinning, the intersection of twin systems, various dislocation activities and the development of grain boundaries during plastic deformation. In some materials, twinning plays an essential role in the subdivision of grains, which can have a beneficial effect on strengthening materials by impeding the movement of dislocations. The grain refinement mechanism provides the basis to accurately describe the deformation responses of materials with complex gradient microstructure.

From a theoretical point of view, the Kocks-Mecking-Estrin (KME) model was developed to describe the evolution of dislocation density with plastic strain rate and grain size (Estrin, 1998; Kocks and Mecking, 2003). Considering dislocation density-based model, some constitutive models have been proposed in the literature to predict the mechanical behaviour of GMS. At the mesoscopic scale, there are two common methods to implement the grain size gradient based on the crystal plasticity finite element simulation method (CPFEM): (a) building grains individually to represent GMS (Chen and Chen, 2018; Yuan and Branicio, 2020; Zeng et al., 2016), and (b) taking grain size-dependent deformation mechanism into a constitutive model (Jin et al., 2018; Lu et al., 2020, 2019). In addition, a constitutive model considering twinning induced plasticity (TWIP) was proposed within the crystal plasticity framework to predict and optimize the mechanical properties of gradient-nanostructured TWIP steels (Lu et al., 2020). At the macroscopic scale, the effects of the combined dislocation density-based and grain size-dependent constitutive model are widely used to analyze the mechanical properties of GMS (Dong et al., 2015; Li and Soh, 2012; Zhao et al., 2022, 2021). The interaction between deformation twinning and grain size has been incorporated into the classical dislocation density-based model to study the influence of twinning, martensitic transformation, and mechanical behaviour on the strength and plasticity of GMS (Latypov et al., 2016; Li et al., 2016; Zhu et al., 2017). To continuously improve the capability of dislocation-based constitutive models, different types of strengthening mechanisms have been taken into account in the evolution of dislocation densities. Densities of geometrically necessary dislocations (GND) and back stress are also considered to describe the deformation of hetero-structured laminated materials (Zhao et al., 2020; Zhao et al., 2021).

These aforementioned methods to model GMS are essentially used when considering the multiscale mechanisms of twinning and martensite transformation of some relevant steels. However, only the gradient grain size and dislocation density are taken into account in these methods (Li and Soh, 2012; Zhao et al., 2021; Zhu et al., 2017), whereas the residual fields of GMS generated during the processes (for example SMAT) such as residual stresses, initial twin volume fraction, twin thickness, etc. are generally not considered. Therefore, to comprehensively and accurately investigate the mechanical properties of GMS generated by mechanical surface treatments, it should be necessary to take these residual fields into account.

In this work, the considered 316L steel GMS is investigated based on Electron Backscatter Diffraction (EBSD) and X-ray diffraction (XRD) observations to assess the residual fields generated by SMAT. Then, these residual fields are numerically expressed with depth-dependent formulations and incorporated into a dislocation density-based constitutive model. This constitutive model is implemented through a user-defined subroutine UMAT of the ABAQUS software. For the further finite element simulations, a two-dimensional (2D) axisymmetric cylindrical model describing a cylindrical structure is considered to analyze the tensile properties of 316L steel processed by SMAT. Particular attention is paid to the influence of residual stress on the mechanical behaviour of the structure under uniaxial tensile loading. To the authors' knowledge, the involvement of residual stress within a gradient structure generated by mechanical surface treatments has not yet been extensively investigated and thus deserves attention.

2. Microstructure obtained by SMAT

During SMAT, due to the presence of a decreased strain gradient and strain rate from the surface induced by impacts, a gradient in grain size, dislocation density, residual stress and twins can be generated (Lu and Lu, 2004). In this work, a dumbbell shape specimen of an austenitic 316L steel is studied, with the following chemical composition (wt%): 0.013C, 1.70Mn, 0.26Si, 0.017P, 0.003S, 17.37Cr, 14.52Ni, 2.8Mo, 0.08Cu, 0.88N, <0.005Ti, 0.07V and balance Fe. The SMAT setup and procedure have been described in previous papers (Wu et al., 2019; Zhou et al., 2021). To highlight the microstructure induced by SMAT, several techniques including EBSD and XRD have been used in the literature (Tao et al., 2002; Zhang et al., 2014).

2.1. Distribution of grain size and twin

EBSD was used in previous works to observe the GMS on the cross-section of SMATed specimens in 316L steel (Benafia et al., 2018; Wu et al., 2019). The EBSD inverse pole figure (IPF) map (Fig. 1) reveals that the SMAT-induced plastic deformation had transformed the material with initially homogeneously distributed grains to a gradient microstructure. The nanocrystalline grain region, transition region, and unaffected bulk region constitute a gradient microstructure. According to the analysis of the EBSD results, it was observed that the grain size exhibits a gradient change from nanograins (about 50 nm in diameter) at the top treated surface to coarse grains (about 10 μm) in the non-affected bulk region. The total thickness of the SMAT affected region is about 200 μm. The nanocrystalline grain region has a thickness of about 5 μm at the top treated surface. It is well known that austenitic steel with low stacking fault energy (SFE) can deform by both glide of individual dislocations and deformation twinning (Bouaziz and Guelton, 2001; Shao et al., 2018). Throughout the generated gradient region, deformation-induced twins along with massive dislocation density generated due to high strain rate can be observed in such a material. However, only annealing twins can be clearly noticed in the unaffected bulk region.

Fig. 1. Microstructure observation on the cross-section of a SMATed specimen in 316L steel by EBSD (Wu et al., 2019).

To precisely describe the mechanical behaviour of the SMATed material, the residual fields, including the grain size, twin thickness, and twin volume fraction, are considered based on experimental measurements. An exponential relationship is widely used to describe the variation in grain size (Li and Soh, 2012; G.-H. Zhao et al., 2020):

$$D = D_c\left(1-\left\{1+\exp\left[\left(z-h_g\right)/c_1\right]\right\}^{-1}\right) \tag{1}$$

where D_c is the grain size of coarse grains in the unaffected bulk region, h_g and c_1 are the fitting constants, and z is the distance from the treated surface. The grain size and strain rate have a strong influence on deformation twinning. Based on experimental results reported in Fig. 1, the twin volume fraction is about 20% in the unaffected region, whereas it is only around 2% in the nanocrystalline grain region. To describe the distribution of twins, the initial twin volume fraction throughout the gradient region is expressed as:

$$f_{t0} = f_{t1} - f_{t2}\exp\left(-z/c_2\right) \tag{2}$$

where f_{t1}, f_{t2}, and c_2 are constants. In the absence of experimental results, the distribution of initial twin thickness is set according to the work performed by (Zhu et al., 2017):

$$D_t = D_{t1} - D_{t2}\exp\left(z/c_3\right) \tag{3}$$

where D_{t1}, D_{t2}, and c_3 are constants.

According to the characteristic values observed from EBSD, the in-depth distributions of grain size, twin thickness, and twin volume fraction are plotted in Fig. 2, by using Eqs. (1-3) with the gradient distribution parameters proposed in Table 1. It shows that the twin thickness is strongly dependent on the grain size. The smallest grains have a lower twin thickness (Ghaderi and Barnett, 2011). Transmission electron microscopy (TEM) observations were made in SMATed austenite 304 SS (Chen et al., 2021), proving that the distribution of twin volume fraction shows a peak shape near the treated surface at about 0.8 µm as shown in Fig. 2b. In the unaffected bulk region, the twin volume fraction keeps a low level, similar to that of the untreated sample. When approaching the treated surface, the increasing strain makes the volume fraction of deformation twin more and more important. However, on one hand, due to the grain refinement mechanism, the deformation twins gradually transformed into grain boundaries, resulting in a rapid decrease in the volume fraction of the existing twins. On the other hand, there are less (or no) twins regenerated at the nanocrystalline grain region because twin nucleation stress was found to increase with decreasing grain size (Rahman et al., 2015). Based on that observation, the peak shape distribution of twin volume fraction is assumed to be the initial twin thickness with a maximum volume fraction of 20% after the SMAT process as shown in Fig. 2b.

Table 1. The parameters of grain size and twinning models.

Parameters (Unit)	Symbols	Values
Grain size function (µm)	D_c, h_g, c_1	10, 90, 18
Volume fraction function (%, %, µm)	f_{t1}, f_{t2}, c_2	20, 20, 38
Twin thickness function (µm)	D_{t1}, D_{t2}, c_3	0.01, 0.01, 39

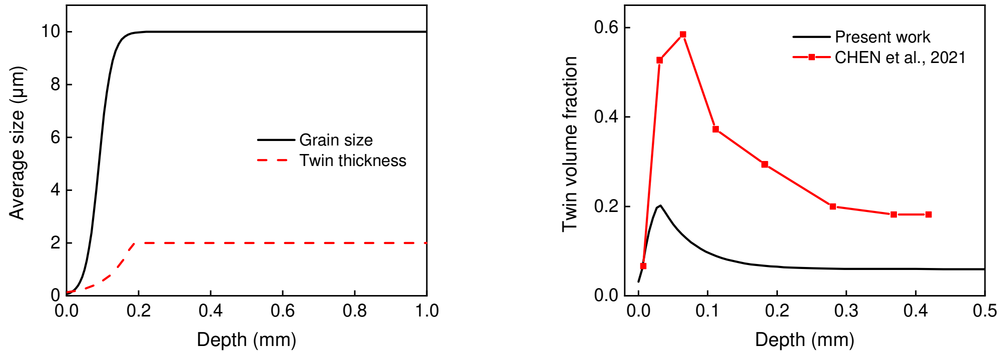

(a) (b)

Fig. 2. In-depth distribution profiles of (a) grain size and twin thickness; (b) twin volume fraction.

2.2. Distribution of residual stress

As mentioned above, a compressive residual stress field is also inevitably generated in GMS by SMAT. It has a significant effect on mechanical behaviour, especially on fatigue properties (Heydari Astaraee et al., 2017). The in-depth variation of the residual stress of a SMATed sample was measured by XRD in a previous work (Zhou et al., 2018). For this purpose, the classical $\sin^2\psi$ method was used. Iterative electrolytic polishing was performed to remove the material layer by layer gradually (Rai et al., 2019). Elastic stress release is especially corrected through stress equilibrium conditions during material removal to obtain the true distribution of in-depth residual stress (Zhou et al., 2021).

Fig. 3 shows the in-depth distribution of residual stress components in the axial and circumferential directions. It can be seen that these residual stresses exhibit remarkable compressive nature with a thickness of about 500 μm, while beyond 500 μm in the bulk region, tensile residual stresses balance the compressive residual stresses for the whole cylindrical structure. Exponential functions based on the stress equilibrium conditions are built to describe the in-depth distribution of residual stresses componentsmm:

$$\begin{cases} \sigma_{zz}^{rs} = \sum_{i=1}^{2} L_i \left(e^{-l_i (r_{\max} - r)} \right) + L_0 \\ \sigma_{\theta\theta}^{rs} = \sum_{i=1}^{2} T_i \left(e^{-t_i (r_{\max} - r)} \right) + T_0 \\ \sigma_{rr}^{rs} = \frac{1}{r} \left[\sum_{i=1}^{2} \frac{T_i}{t_i} \left(e^{-t_i (r_{\max} - r)} - 1 \right) - T_0 \left(r_{\max} - r \right) \right] \end{cases} \tag{4}$$

where L_0, L_i, l_i, T_0, T_i and t_i are constants fitted from the residual stress profiles presented in Fig. 3. Table 2 lists the values of the parameters involved in Eqs. (4).

Table 2. The parameters of residual stress reconstruction model.

Axial					Circumferential				
L_1 (MPa)	l_1 (m^{-1})	L_2 (MPa)	l_2 (m^{-1})	L_0 (MPa)	T_1 (MPa)	t_1 (m^{-1})	T_2 (MPa)	t_2 (m^{-1})	T_0 (MPa)
10547.64	6.95	-11303.32	6.19	188.58	315.23	17.36	-832.24	2.84	91.60

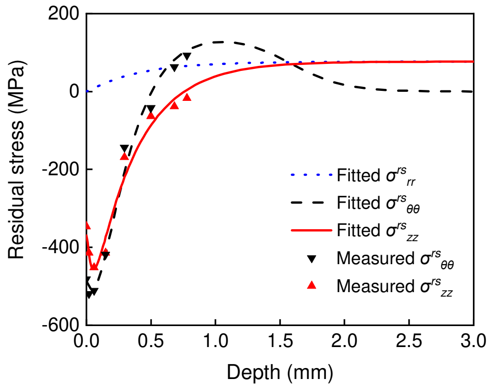

Fig. 3. In-depth distribution of residual stress after SMAT.

It is worthwhile to note that there is no martensitic transformation after SMAT, in the present case, according to the obtained XRD patterns of as-received and SMATed samples (Zhou, 2018).

2.3. Distribution of initial dislocation density

It is well documented that there is a link between accumulated plastic strain and dislocation density. This link can be built through the relation expressed in Eq. 5 (Williamson and Smallman, 1956).

$$\rho_0 = 2\sqrt{3}\frac{\varepsilon_{rs}^{p}}{bD} \tag{5}$$

where b is the magnitude of Burgers vector, ε_{rs}^{p} is the residual accumulated plastic strain. In a previous study (Zhou et al., 2018), the residual accumulated plastic strain was assessed from the full width at half maximum (FWHM) of XRD peaks. Fig. 4 shows the distributions of accumulated plastic strain and initial dislocation density in the near-surface SMAT affected region. In this figure, the experimental data of initial dislocation density from (Ghosh et al., 2021) are also given in red points for comparison. It can be seen that the accumulated plastic strain gradually decreases from the treated surface to the bulk. This plastic strain gradient is gradually formed in the near-surface region during the SMAT process. This observation of accumulated plastic strain is consistent with Fig. 1, which shows a fairly large near-surface region mechanically affected by SMAT due to high strain rate impacts. Based on Eq. (5), it can also be seen that initial dislocation density has a similar tendency, but varies more sharply with distance from the surface.

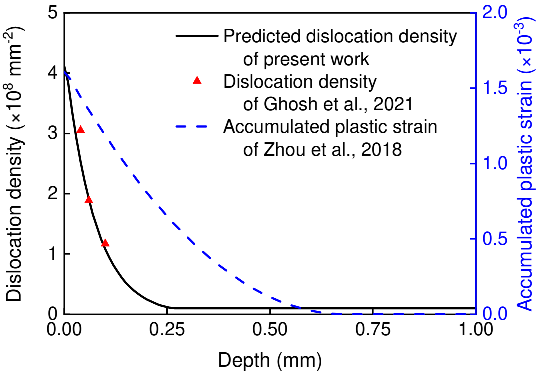

Fig. 4. In-depth distribution profiles of initial dislocation density and accumulated plastic strain.

3. Constitutive model for GMS

The involvement of multiple acting factors including residual stress, dislocation, and twinning lead to a complex plastic deformation behaviour during tensile loading. For the investigation of the mechanical behaviour of GMS, a combined dislocation density-based and depth-dependent constitutive model is established based on the elastoplastic framework. In addition, the experimental residual fields, expressed as depth-dependent formulations in Section 2, are also taken into account in the model as initial conditions through a user-defined subroutine UMAT.

3.1. Evolution of yield stress

Generally, the refined-grains and large quantities of dislocations are two major sources of strengthening in GMS. The increase in yield stress caused by grain boundaries can be estimated by the Hall-Petch model. It is noted that there can be a limitation of grain boundary strengthening due to the grain rotation and grain boundary sliding processes when the grain size is reduced to the nanoscale (Liu et al., 2015; Zhu et al., 2004). In addition, the well-known Taylor relationship can be used to describe the increase in yield stress σ_y caused by the isotropic hardening related to the intragranular dislocation interactions. Therefore, the yield stress evolution can be determined with the contributions of stored dislocations and grain size:

$$\sigma_y = \sigma_0 + \frac{k_{HP}}{\sqrt{D}} + M\alpha\mu b\sqrt{\rho} \tag{6}$$

where σ_0 is the lattice friction stress (corresponding to initial yield strength at microscopic scale) ; k_{HP} is the Hall-Petch slope; D is the grain size; M is the Taylor factor; α is a material constant around 0.3; b is the Burgers vector norm. μ is the shear modulus; ρ is the dislocation density. Before loading, the initial yield stress at each depth can be calculated by Eq. (6), when the dislocation density equals the initial dislocation density ρ_0 in Eq. (5).

3.2. Evolution of dislocation density including twinning

Deformation twinning is a common mechanism of plastic deformation, especially in austenitic steels with low SFE. The macroscopic strain ε and shear strain γ are linked to the Taylor factor as follows: $\varepsilon = \gamma/M$. To take into account the contribution of twinning, the total strain increment $d\varepsilon$ can be expressed by the mixture law incorporating dislocation slip and twinning contributions:

$$d\varepsilon = (1-f_t)\,d\varepsilon_s + \varepsilon_t df_t \tag{7}$$

where ε_s is the strain caused by dislocation slip, ε_t is the strain associated with twinning. The shear strain of twinning γ_t is $1/\sqrt{2}$ (Bouaziz et al., 2011). Rearranging the expressions described by Eqs. (6) and (7), it gives:

$$\frac{d\varepsilon_s}{d\varepsilon} = \frac{1}{1-f_t}\left(1-\frac{\gamma_t}{M}\frac{df_t}{d\varepsilon}\right) \tag{8}$$

where M is the Taylor factor, f_t is the twin volume fraction, which is an assumption expressed as follows (Allain et al., 2004; Bouaziz and Guelton, 2001):

$$f_t = F_{\max}\left(1-\mathrm{e}^{-\beta(\varepsilon-\varepsilon_{t0})}\right)^m \quad , \quad \varepsilon > \varepsilon_{t0} \tag{9}$$

where F_{max} is the maximum twin fraction, β is the twinning kinetics parameter, and m is the intensity parameter of the TWIP effect, ε_{t0} is the critical strain for twinning initiation. It should be noticed that the sensibility of grain size on the twin volume fraction depends on the SFE of the material (Ghaderi and Barnett, 2011). It means that the twinning kinetics parameter β in Eq. 9 is grain size-dependent. By differentiating Eq. (9), the twin volume fraction rate can be obtained as:

$$\frac{df_t}{d\varepsilon}=F_{max}\beta m\exp\left[-\beta\left(\varepsilon-\varepsilon_{t0}\right)\right]\left\{1-\exp\left[-\beta\left(\varepsilon-\varepsilon_{t0}\right)\right]\right\}^{m-1} \tag{10}$$

Dynamic accumulation and annihilation of dislocation processes were taken into account in the classical KME model. The rate of dislocation storage is inversely related to the dislocation mean free path Λ, which depends on the multiplication of dislocations, the twin spacing, and the dislocation forest induced by dislocation interactions. The deformation-induced twins positively affect the work-hardening by impeding the gliding movement of dislocations through twinning boundaries. Accordingly, the generalized equation for the rate of forest dislocation evolution with strain can be expressed as:

$$\frac{d\rho^+}{d\varepsilon_s}=\frac{M}{\Lambda b}=\frac{M}{b}\left(\frac{1}{D}+\frac{1}{t}+k_1\sqrt{\rho}\right) \tag{11}$$

where k_1 is a geometric factor related to grain boundary and dislocation forest. The average twin spacing t is related to the twin thickness D_t and the twin volume fraction f_t given by:

$$\frac{1}{t}=\frac{1}{2D_t}\cdot\frac{f_t}{1-f_t} \tag{12}$$

On the other hand, grain boundaries play an important role in strain hardening with decreasing grain size, especially in refined-grains. However, the classical KME model only considers dislocation annihilation due to dynamic recovery. The grain size effect was observed in nanocrystallization grain in SMATed Fe sample (Lu and Lu, 2004), it was reported that the deformation mechanism was no longer governed by accumulation of dislocations, but by the grain rotation or grain boundary sliding processes when the grain size is reduced to few nanometers. For this purpose, an additional dynamic grain size-related recovery term is added to describe the decrease in work hardening due to grain refinement (Li and Soh, 2012):

$$\frac{d\rho^-}{d\varepsilon_s}=-M\rho\left[k_{20}\left(\frac{\dot{\varepsilon}^p}{\dot{\varepsilon}_0}\right)^{-\frac{1}{n_0}}-\left(\frac{D_e}{D}\right)^2\right] \tag{13}$$

where k_{20} is the dynamic recovery constant, n_0 is an exponent inversely proportional to temperature, $\dot{\varepsilon}_0$ is the reference strain rate, and D_e is the reference grain size. It should be noted that the parameter n_0 is related to the SFE, which may affect the generation of GND and grain refinement during SMAT. A SMATed sample with high SFE has stronger back stress hardening and smaller grain sizes (Galindo-Nava and Rivera-Díaz-del-Castillo, 2017; Sinha et al., 2015; Zhang et al., 2019; G.-H. Zhao et al., 2020). It is noticed that the rate term involving the calculation of flow stress in Eq. 6 is not considered in Newton's iterative implementation.

Combining Eqs. (8), (11) and (13), the evolution of the dislocation density can be expressed with respect to the total strain ε:

$$\frac{d\rho}{d\varepsilon}=\frac{d\rho}{d\varepsilon_s}\frac{d\varepsilon_s}{d\varepsilon}=\left(\frac{d\rho^+}{d\varepsilon_s}+\frac{d\rho^-}{d\varepsilon_s}\right)\frac{d\varepsilon_s}{d\varepsilon}=$$
$$\frac{1}{1-f_t}\left(M-\frac{1}{\sqrt{2}}\frac{df_t}{d\varepsilon}\right)\left[\frac{1}{b}\left(\frac{1}{D}+\frac{1}{t}+k\sqrt{\rho}\right)-k_{20}\left(\frac{\dot{\varepsilon}^p}{\dot{\varepsilon}_0}\right)^{-\frac{1}{n_0}}\rho-\left(\frac{d_e}{d}\right)^2\rho\right] \tag{14}$$

4. Finite element simulation

The constitutive model described in Section 3 is used to predict the tensile response of GMS with the residual fields expressed in Section 2 by the commercial FE software ABAQUS. The hardening of GMS is governed by the deformation twinning and dislocation density. The depth-dependent functions describing the residual fields generated by SMAT are considered in the UMAT subroutine according to Eqs. (1)-(5). Meanwhile, the residual stresses are introduced at the beginning of the simulation through the SIGINI subroutine. Then, the constitutive model in the plasticity framework with isotropic hardening is assigned to the whole finite element (FE) model.

4.1. FE model for tensile simulation

As shown in Fig. 5a, the central section of the cylindrical sample after SMAT is taken as the part of interest. In order to reduce the solving time, a representative 2D-axisymmetric model is built to analyze the tensile properties of GMS. The symmetry boundary condition is applied to the cross-section. To simulate the uniaxial tensile test, a displacement is applied to the upper border of GMS through coupling constraint. The model is meshed by using four-node axisymmetric elements (CAX4). The mesh size from 5 μm (at the treated surface) to 100 μm (in the bulk) was adopted for the FE model as shown in Fig. 5b. The material parameters for GMS are identified by microstructural observations or from the literature, as listed in Table 3.

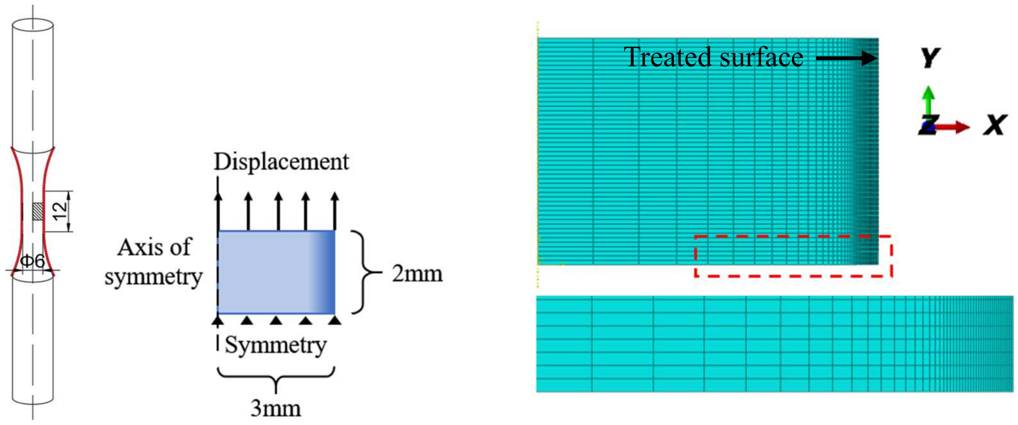

(a) (b)

Fig. 5. Section of a SMATed sample: (a) geometrical model and boundary conditions, (b) FE model showing the mesh.

Table 3 Material parameters for the model of GMS

Symbols	Parameters	Values
σ_0 (MPa)	Lattice frictional stress	70 (Chen et al., 2005)
K_{HP} (MPa·m$^{1/2}$)	Hall–Petch slope	0.25 (Chen et al., 2005)
M	Taylor factor	3.06 (Li and Soh, 2012)
α	Taylor constant	0.3 (Li and Soh, 2012)
μ (GPa)	Shear modulus	82 (Ghosh et al., 2021)
b (nm)	Magnitude of Burgers vector	0.256 (Li and Soh, 2012)
F_{max}	Maximum twin fraction	0.35 (Liu et al., 2010)
β	Twinning kinetics parameter	8 (G.-H. Zhao et al., 2020)
m	Twinning intensity parameter	1.2 (G.-H. Zhao et al., 2020)
ε_{t0}	Critical strain for twinning initiation.	0.05 (Sinha et al., 2015)
k_1	Proportionality factor	0.026 (J. Zhao et al., 2020)
k_{20}	Dynamic recovery constant 1	2.5 (Li and Soh, 2012)
n_0	Dynamic recovery constant 2	21.25 (Li and Soh, 2012)
$\dot{\varepsilon}_0$ (s^{-1})	Reference strain rate	1 (Li and Soh, 2012)
d_e (nm)	Reference grain size	580 (Li and Soh, 2012)

4.2. Validation of stress-strain relationship and yield strength

Fig. 6 displays the yield strength evolution with the grain size of GMS. It can be seen that the yield strength significantly increases with grain size due to the combination of grain boundary strengthening effect and dislocation interaction. The yield strength in the nanocrystalline region σ_{gs} can reach 1277 MPa, whereas the yield strength in the bulk region σ_{bulk} is only 270 MPa, which is consistent with experimental results (Chen et al., 2005; Ghosh et al., 2021; Kashyap, 1997; Üçok et al., 1991).

In addition, the calculated local mechanical behaviour of the nanocrystalline and the coarse grains (with grain sizes: 50 nm and 10 µm, respectively) are shown in Fig. 7a. Experimental data on stress-strain relations obtained by (Chen et al., 2005) are also presented by circular dots in the same figure for comparison. The elastic stiffness of nanocrystalline and coarse grain materials is assumed to be grain size-independent. Therefore, the two curves have the same slope at the elastic deformation stage. When comparing the plastic stage, the calculated results are in rather good agreement with the experimental measurements.

Fig. 7b displays the overall true stress-strain curves of untreated structure and GMS with and without residual stress during uniaxial tension. In comparison, the yield strength is 312 MPa for the GMS without residual stress and 297 MPa for the GMS with residual stress. It shows that the residual stresses can slightly decrease the yield stress of GMS, this curvature effect agrees with the tensile properties of SMATed TA6V sample (Roland, 2006). In addition, the yield strength of GMS is slightly higher than the untreated material (270 MPa). Because of the relatively thin thickness of the GMS layer in this work, the influence of strengthening by SMAT is not very significant on the tensile behaviour. As mentioned above, the thickness of the nanocrystalline layer is about 5 µm at the treated surface, and the volume fraction of the nanocrystalline layer f_{gs} represents only 0.33% of the cylindrical structure. These yield stress results are basically consistent with the simple law of mixture $\bar{\sigma}_y = f_{gs}\sigma_{gs} + (1 - f_{gs})\sigma_{bulk} = 273.8$ MPa. In other words, the volume fraction of GMS can directly influence the global tensile behaviour at the macroscopic scale. The multiple strengthening mechanisms in the gradient-nanocrystallized grain materials provide higher mechanical strength than the untreated sample.

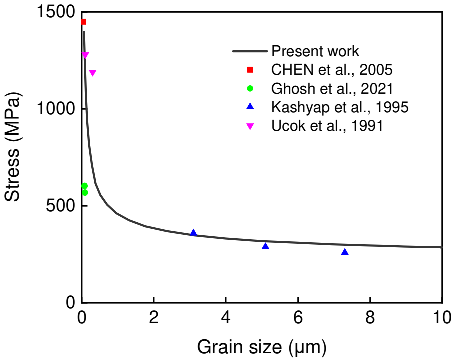

Fig. 6. Comparison between numerical and experimental results on the yield strength versus grain size.

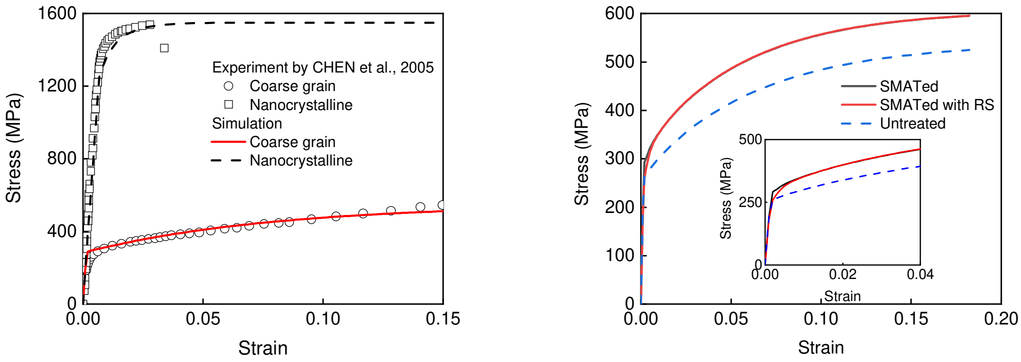

(a) (b)

Fig. 7. (a) Comparison of predicted local strain-stress curves between nanocrystalline and coarse grains, and (b) comparison of predicted global strain-stress curves between untreated structure and GMS during uniaxial tensile loading (RS = residual stress).

5. Results and discussion

By using the parameters provided in Table 3, the stress-strain relationship and yield strength of the GMS can be calculated based on the models presented above. The tensile simulations are an effective way to understand the stretching process during plastic deformation of the near-surface region. After simulations, four representative depths (associated with different grain sizes: 50 nm, 250 nm, 2 μm, and 10 μm) are chosen to illustrate the mechanical properties and the evolutions of twin volume fraction and dislocation density of GMS.

5.1. Effect of residual stress in GMS

The tensile simulations with and without residual stresses are performed to evaluate the effect of compressive residual stresses on the mechanical responses of GMS. Fig. 8a illustrates the von Mises stress distribution obtained by FE simulation for the GMS. The GMS, which wraps the unaffected bulk region, constrains the deformation along the tensile direction. It causes a high-level stress (1592 MPa) at the surface. The simulated local mechanical behaviour of GMS with and without residual stress is given by solid and dashed curves in Fig. 8b, respectively. In comparison, it can be observed that the residual stress mainly influences the mechanical behaviour at the initial stage of deformation. As the strain increases, there is little influence on the tensile mechanical behaviour with different grain sizes. This is due to the fact that residual stress is internally balanced throughout the whole structure during the plastic deformation, which is similar to the overall mechanical behaviour at different grain sizes as shown in Fig. 7b. Specifically, in the low strain level, most of the externally imposed deformation is accommodated by the interior coarse grains.

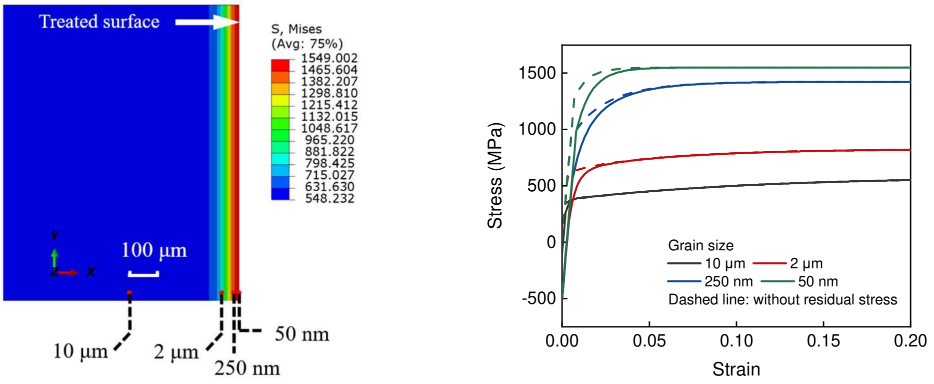

(a) (b)

Fig. 8. (a) Distributions of von Mises stress after tensile loading, and (b) strain-stress curves at different grain sizes with residual stress (in solid line) and without residual stress (in dashed line).

As mentioned above, the SMATed structure presents a gradient yield strength in the near-surface region, which results in inhomogeneous deformation during tensile loading as shown in Fig. 9. During tensile loading, the deformation spreads outward from the soft coarse grains to the nanocrystallized grains. In the early stages of deformation, due to the gradient yield strength, the coarse grains in the bulk started to present a plastic deformation, whereas the nanocrystallized grains in the surface layer remain elastically deformed. That elastic/plastic transition throughout the near-surface SMAT affected region could generate a large strain gradient, which consequently leads to a high level of GND at the early deformation stage (Samih et al., 2013). It should be noted that the tensile stresses internally cause stronger deformation in the corresponding coarse grain region.

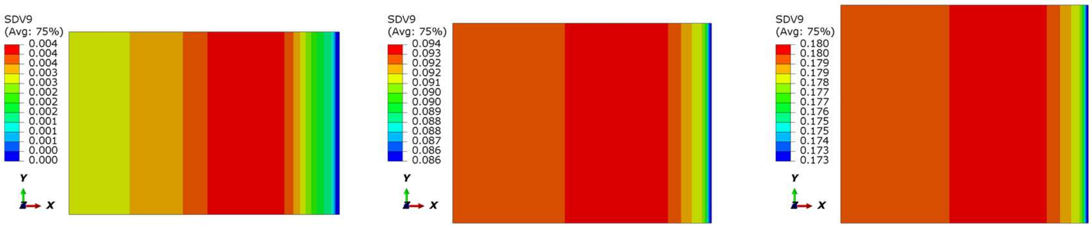

ε=0.005 ε=0.1 ε=0.2

Fig. 9. Evolution of equivalent plastic strain during tensile loading (at a strain of 0.2 along Y-axis).

5.2. Predicted evolution of the twin volume fraction

It can be seen from the distribution of initial twin volume fraction in Fig. 10a that the points of grain size 50 nm and 250 nm are located on the right side of peak value, whereas the points of grain size 2 μm and 10 μm are situated on the left on the opposite side. The SMAT process refines the grains down to the nanoscale (ranging from 50 nm to 250 nm) in the near-surface region, and meanwhile the existing twin structure is destroyed by the grain refinement effect. Almost no twin can be distinguished in nanocrystallized grains in a SMATed 316L sample (Sun et al., 2017). As mentioned above, each side has a different mechanism on the evolution of deformation twinning, accumulated on the left side and transformed to grain boundaries on the other side. It is noticed that the constitutive model used in the present work does not implement the grain refinement with increase of dislocations and twins in the microscale.

In addition to the twin nucleation, twin volume fraction strongly depends on the grain size in slip-dominated materials (Ghaderi and Barnett, 2011). Therefore, grain size-dependent twin volume fraction is considered by the factor β in this model and assumed in Eq. 15, which will need further experimental study.

$$\begin{aligned} &\beta = \beta_0 \times coefficient(D) \\ &coefficient(D) = \left(D / D_{e2}\right)^2 \end{aligned} \tag{15}$$

where β_0 is the basic twinning kinetics parameter and D_{e2} is the reference grain size for twinning. Fig. 10b shows the evolution of twin volume fractions at different depths (i.e., with varying grain sizes) with the increase in plastic strain during tensile loading. It can be seen that during tensile loading, the twin volume fraction increases with strain in coarse grains. The twin volume fraction significantly increases from 6.0% to 30.2% at grain size 10 μm, and increases slightly from 13.3% to 14.5% at grain size 2 μm. However, the twin volume fraction in nanocrystallized grains barely changes during tensile loading and keeps the initial state obtained by SMAT. It means that the deformation twinning is inactive in nanocrystallized grains during tensile loading.

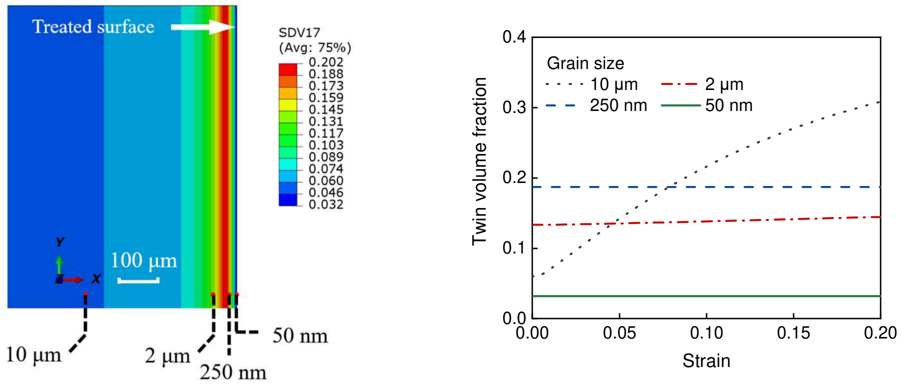

(a) (b)

Fig. 10. (a) Distributions of initial twin volume fraction (b) Predicted evolution of twin volume

fraction with different grain sizes (corresponding to different depths beneath the SMATed surface).

5.3. Dislocation density distribution within GMS

As mentioned in Section 3, TWIP and grain size effects are integrated into a dislocation density-based constitutive model to describe the mechanical properties of a SMATed sample. Fig. 11a shows the distribution of such dislocation density after tensile loading simulation. The maximum dislocation density reaches 18.9×10^8 mm^{-2} at the sub-surface. At the treated surface, the significant reduction in dislocation density is caused by dynamic recovery expressed by Eq. (13). Therefore, the maximum dislocation density is located in the sub-surface.

The evolution of dislocation density during tensile loading of the GMS is presented in Fig. 11b with different grain sizes. On one hand, since the SMAT introduces a gradient density of strain-induced dislocations in the region of the treated surface, this region has a higher residual dislocation density than the coarse grain bulk before deformation. On the other hand, as mentioned above, different grain sizes are associated with different yield strengths, which causes inhomogeneous deformation. The smaller grain size (with higher yield strength) delays elastic-plastic transition, which prolongs simultaneously the turning point of dislocation density. With the increase in plastic strain, the dislocation density increases from 4.8×10^8 mm^{-2} to 8.6×10^8 mm^{-2} at the treated surface, and from 1.3×10^8 mm^{-2} to 4.4×10^8 mm^{-2} in the central bulk region. As the strain increases even further, the dislocation density gradually saturates, especially in the nanocrystallized layer.

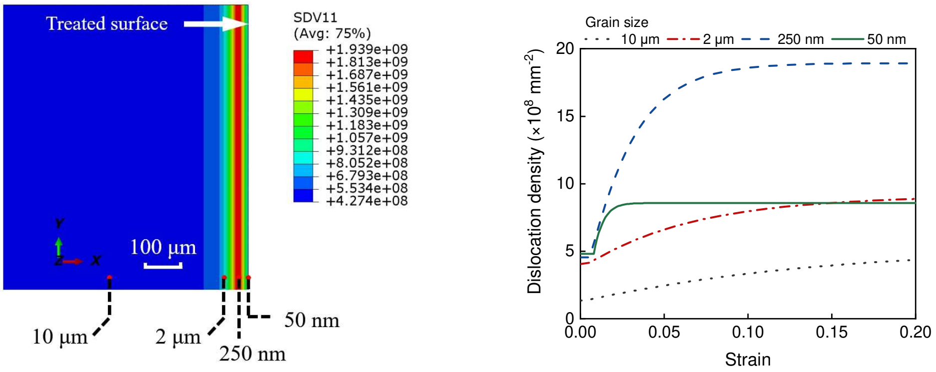

(a) (b)

Fig. 11. (a) Distribution of dislocation density after tensile loading, and (b) predicted evolution of dislocation density with different grain sizes.

5.4. Effect of deformation twinning in GMS

Four different twinning conditions are set to study the twinning influence on the mechanical property of GNS. (I): No twinning mechanism involved in the constitutive model as comparison; (II): Normal twinning as mentioned above; (III): No initial twinning fraction induced during loading; (IV): Massive twinning generated by increasing the basic twinning kinetics parameter β_0 in Eq. (15). Fig. 12 shows the evolution of twin volume fraction with different twinning conditions for different grain sizes. By comparison of the normal and massive conditions, it can be seen that the twin volume fraction of the massive twinning gradient increases more than the normal one with increasing strain. However, the twin volume fraction has almost no variation and is equal to the initial value of all conditions for grain sizes 250 nm and 50 nm. In addition, the no initial and normal conditions have the same tendency, but translate the value of the initial twin volume fraction.

It can be seen from Fig. 13, the evolution of dislocation density and strain-stress curves have the same change rule with twin volume fraction. During tensile loading, the twin volume fraction increases with strain, simultaneously associated with increased dislocation density and strain hardening, to accommodate the excess strain from external loading (Shao et al., 2018).

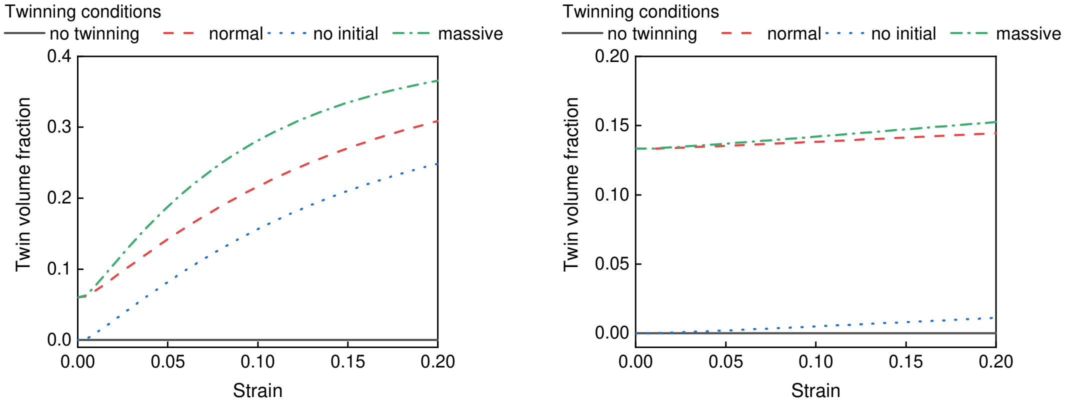

(a) 10 μm (b) 2 μm

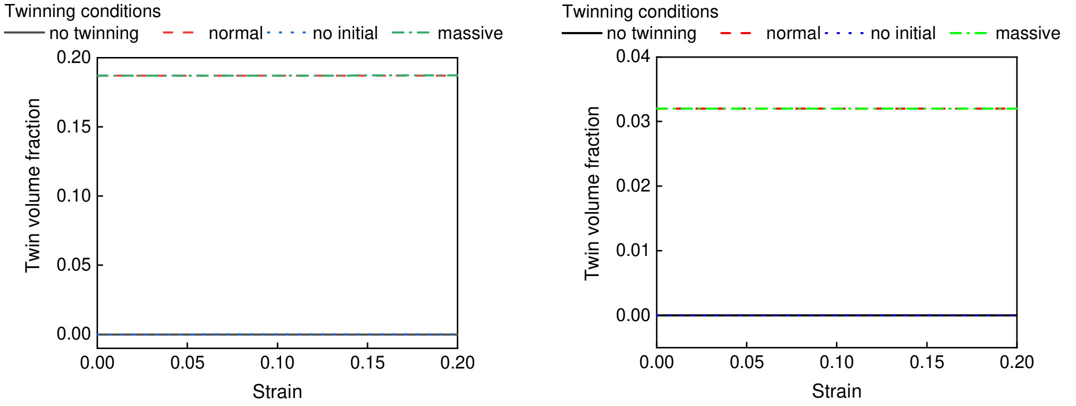

(c) 250 nm (d) 50 nm

Fig. 12. Evolution of twin volume fraction with different twinning conditions at different grain sizes.

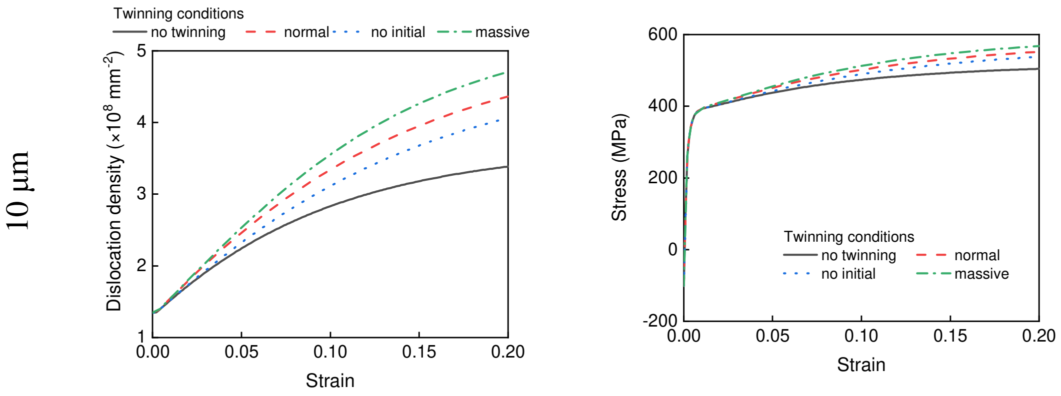

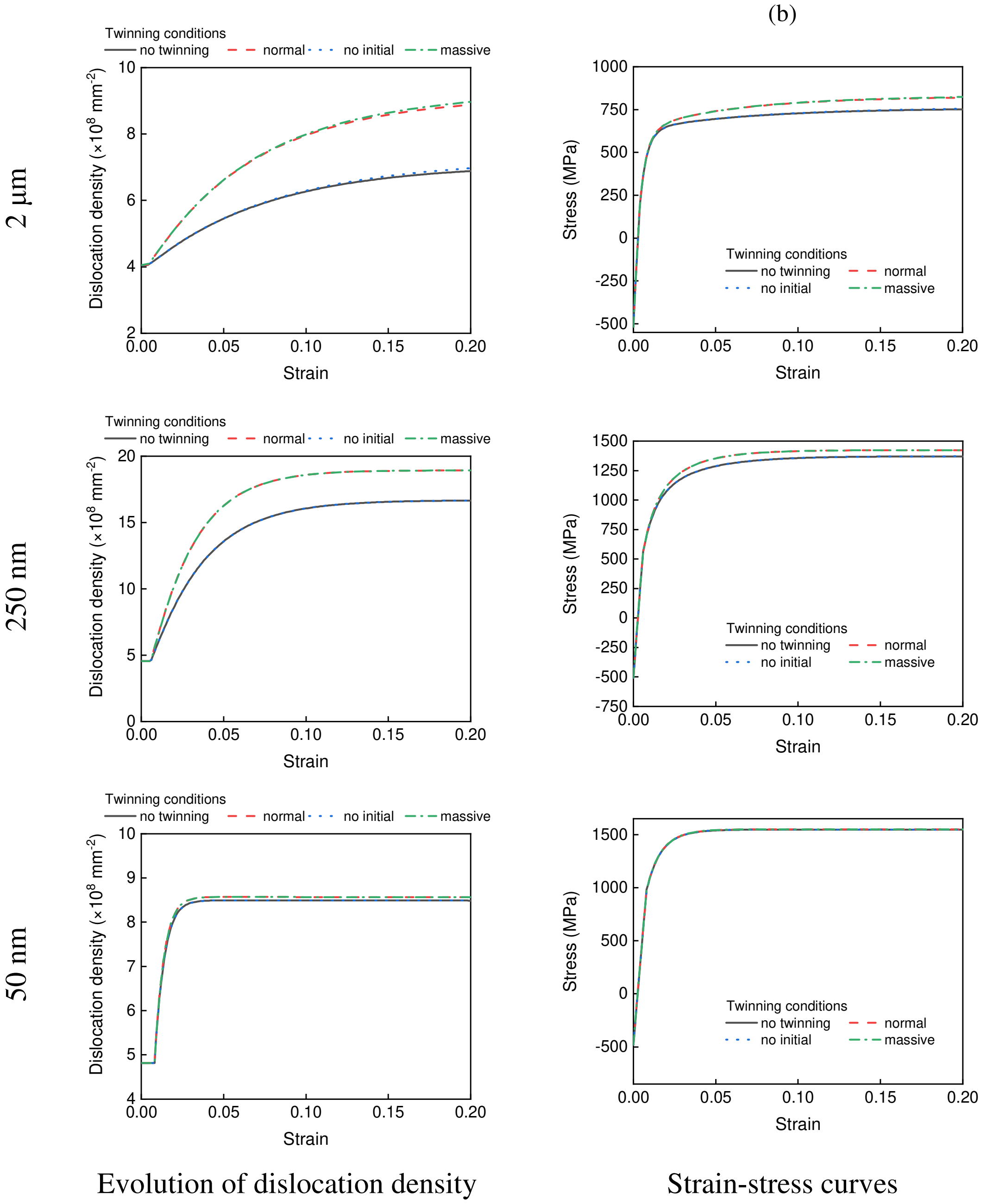

Fig. 13. Predicted evolution of dislocation density and strain-stress curves with four different grain sizes (10 μm, 2 μm, 250 nm and 50 nm).

6. Conclusion

In this work, a combined dislocation density-based and depth-dependent constitutive model involving microstructural parameters is built to describe the mechanical behaviour of GMS at the macroscopic scale. In addition, the depth-dependent residual fields (grain size, residual stress, dislocation density, and twinning) are considered in the FE model of a cylindrical structure. Based on the obtained results, the following conclusions can be drawn:

- Compared with experimental results, the developed theoretical model is able to describe correctly the mechanical properties of the GMS obtained by SMAT.
- The GMS induced by SMAT presents inhomogeneous deformation. The coarse

grains in the bulk started with plastic deformation, whereas the nanocrystallized grains in the surface layer still deformed elastically. At a low strain level, the interior coarse grains accommodated most of the externally imposed deformation.

- The dislocation densities and twin volume fractions of layers with different grain sizes increase rapidly and gradually saturate during tensile loading.
- Detailed analysis of the local and overall tensile behaviour of GMS found that superficial compressive residual stress generated by SMAT plays a significant role in decreasing the yield strength mainly at the initial stage of deformation. However, with increasing of deformation, the residual stresses barely have less influence on the tensile behaviour, since the residual stress is always internally balanced as the deformation proceeds. In addition, due to the gradient feature of residual stress, its influence gradually decreases with increasing depth.
- The simulation results revealed that the twin volume fraction increases in coarse grains, but barely changes and keeps the initial state in nanocrystallized grains during tensile loading.

In future work, more precise modelling of the gradient structure coupled with residual stress field will be achieved in order to perform a more quantitative analysis of structures processed by mechanical surface treatments.

Acknowledgments

Z. GUO gratefully acknowledges the financial support from the China Scholarship Council (CSC).

Data availability

The raw/processed data required to reproduce these findings cannot be shared at this time as the data also forms part of an ongoing study.

References

Allain, S., Chateau, J.-P., Bouaziz, O., 2004. A physical model of the twinning-induced plasticity effect in a high manganese austenitic steel. Mater. Sci. Eng. A 387–389, 143–147. https://doi.org/10.1016/j.msea.2004.01.060

An, Y., Du, H., Wei, Y., Wang, N., Hou, L., Lin, W., 2013. Interfacial structure and mechanical properties of surface iron–nickel alloying layer in pure iron fabricated by surface mechanical attrition alloy treatment. Mater. Des. 46, 627–633. https://doi.org/10.1016/j.matdes.2012.11.005

Ao, N., Liu, Daoxin, Xu, X., Zhang, X., Liu, Dan, 2019. Gradient nanostructure evolution and phase transformation of α phase in Ti-6Al-4V alloy induced by ultrasonic surface rolling process. Mater. Sci. Eng. A 742, 820–834. https://doi.org/10.1016/j.msea.2018.10.098

Bahl, S., Suwas, S., Ungàr, T., Chatterjee, K., 2017. Elucidating microstructural evolution and strengthening mechanisms in nanocrystalline surface induced by surface mechanical attrition treatment of stainless steel. Acta Mater. 122, 138–151. https://doi.org/10.1016/j.actamat.2016.09.041

Benafia, S., Retraint, D., Yapi Brou, S., Panicaud, B., Grosseau Poussard, J.L., 2018. Influence of Surface Mechanical Attrition Treatment on the oxidation behaviour of 316L stainless steel. Corros. Sci. 136, 188–200. https://doi.org/10.1016/j.corsci.2018.03.007

Bouaziz, O., Allain, S., Scott, C.P., Cugy, P., Barbier, D., 2011. High manganese austenitic twinning induced plasticity steels: A review of the microstructure properties relationships. Curr. Opin. Solid State Mater. Sci. 15, 141–168. https://doi.org/10.1016/j.cossms.2011.04.002

Bouaziz, O., Guelton, N., 2001. Modelling of TWIP effect on work-hardening. Mater. Sci. Eng. A 319–321, 246–249. https://doi.org/10.1016/S0921-5093(00)02019-0

Cai, B., Ma, X., Moering, J., Zhou, H., Yang, X., Zhu, X., 2015. Enhanced mechanical properties in Cu–Zn alloys with a gradient structure by surface mechanical attrition treatment at cryogenic temperature. Mater. Sci. Eng. A 626, 144–149. https://doi.org/10.1016/j.msea.2014.12.070

Chen, A., Wang, C., Jiang, J., Ruan, H., Lu, J., 2021. Microstructure Evolution and Mechanical Properties of Austenite Stainless Steel with Gradient Twinned Structure by Surface Mechanical Attrition Treatment. Nanomaterials 11, 1624. https://doi.org/10.3390/nano11061624

Chen, D., Mao, X., Ou, M., Liang, Y., 2022. Mechanical properties of gradient structured copper obtained by ultrasonic surface rolling. Surf. Coat. Technol. 431, 128031. https://doi.org/10.1016/j.surfcoat.2021.128031

Chen, X.H., Lu, J., Lu, L., Lu, K., 2005. Tensile properties of a nanocrystalline 316L austenitic stainless steel. Scr. Mater. 52, 1039–1044. https://doi.org/10.1016/j.scriptamat.2005.01.023

Chen, Z., Chen, Y., 2018. Nanocrystalline gradient engineering: Grain evolution and grain boundary networks. Comput. Mater. Sci. 141, 282–292. https://doi.org/10.1016/j.commatsci.2017.09.047

Darling, K.A., Rajagopalan, M., Komarasamy, M., Bhatia, M.A., Hornbuckle, B.C., Mishra, R.S., Solanki, K.N., 2016. Extreme creep resistance in a microstructurally stable nanocrystalline alloy. Nature 537, 378–381. https://doi.org/10.1038/nature19313

Deng, S.Q., Godfrey, A., Liu, W., Hansen, N., 2016. A gradient nanostructure generated in pure copper by platen friction sliding deformation. Scr. Mater. 117, 41–45. https://doi.org/10.1016/j.scriptamat.2016.02.007

Dong, S., Zhou, J., Hui, D., Wang, Y., Zhang, S., 2015. Size dependent strengthening mechanisms in carbon nanotube reinforced metal matrix composites. Compos. Part Appl. Sci. Manuf. 68, 356–364. https://doi.org/10.1016/j.compositesa.2014.10.018

Dureau, C., Arzaghi, M., Massion, R., Nadot, Y., Grosdidier, T., 2022. On the high cycle fatigue resistance of austenitic stainless steels with surface gradient microstructures: Effect of load ratio and associated residual stress modification. Mater. Sci. Eng. A 840, 142916. https://doi.org/10.1016/j.msea.2022.142916

Estrin, Y., 1998. Dislocation theory based constitutive modelling: foundations and applications. J. Mater. Process. Technol. 80–81, 33–39. https://doi.org/10.1016/S0924-0136(98)00208-8

Galindo-Nava, E.I., Rivera-Díaz-del-Castillo, P.E.J., 2017. Understanding martensite and twin formation in austenitic steels: A model describing TRIP and TWIP effects. Acta Mater. 128, 120–134. https://doi.org/10.1016/j.actamat.2017.02.004

Ghaderi, A., Barnett, M.R., 2011. Sensitivity of deformation twinning to grain size in titanium and magnesium. Acta Mater. 59, 7824–7839. https://doi.org/10.1016/j.actamat.2011.09.018

Ghosh, S., Bibhanshu, N., Suwas, S., Chatterjee, K., 2021. Surface mechanical attrition treatment of additively manufactured 316L stainless steel yields gradient nanostructure with superior strength and ductility. Mater. Sci. Eng. A 820, 141540. https://doi.org/10.1016/j.msea.2021.141540

Ghosh, S., Kain, V., 2010. Microstructural changes in AISI 304L stainless steel due to surface machining: Effect on its susceptibility to chloride stress corrosion cracking. J. Nucl. Mater. 403, 62–67. https://doi.org/10.1016/j.jnucmat.2010.05.028

Heydari Astaraee, A., Miresmaeili, R., Bagherifard, S., Guagliano, M., Aliofkhazraei, M., 2017. Incorporating the principles of shot peening for a better understanding of surface mechanical attrition treatment (SMAT) by simulations and experiments. Mater. Des. 116, 365–373. https://doi.org/10.1016/j.matdes.2016.12.045

Jin, H., Zhou, J., Chen, Y., 2018. Grain size gradient and length scale effect on mechanical behaviors of surface nanocrystalline metals. Mater. Sci. Eng. A 725, 1–7. https://doi.org/10.1016/j.msea.2018.03.103

Kashyap, B., 1997. Hall-Petch relationship and substructural evolution in boron containing type 316L stainless steel. Acta Mater. 45, 2383–2395. https://doi.org/10.1016/S1359-6454(96)00341-2

Kocks, U.F., Mecking, H., 2003. Physics and phenomenology of strain hardening: the FCC case. Prog. Mater. Sci. 48, 171–273. https://doi.org/10.1016/S0079-6425(02)00003-8

Latypov, M.I., Shin, S., De Cooman, B.C., Kim, H.S., 2016. Micromechanical finite element analysis of strain partitioning in multiphase medium manganese TWIP+TRIP steel. Acta Mater. 108, 219–228. https://doi.org/10.1016/j.actamat.2016.02.001

Lei, L., Zhao, Q., Zhao, Y., Wu, C., Huang, S., Jia, W., Zeng, W., 2022. Gradient nanostructure, phase transformation, amorphization and enhanced strength-plasticity synergy of pure titanium manufactured by ultrasonic surface rolling. J. Mater. Process. Technol. 299, 117322. https://doi.org/10.1016/j.jmatprotec.2021.117322

Li, J., Soh, A.K., 2012. Modeling of the plastic deformation of nanostructured materials with grain size gradient. Int. J. Plast. 39, 88–102. https://doi.org/10.1016/j.ijplas.2012.06.004

Li, L., Liu, S., Ye, B., Hu, S., Zhou, Z., 2016. Quantitative analysis of strength and plasticity of a 304 stainless steel based on the stress-strain curve. Met. Mater. Int. 22, 391–396. https://doi.org/10.1007/s12540-016-5466-2

Liu, G.Z., Tao, N.R., Lu, K., 2010. 316L Austenite Stainless Steels Strengthened by Means of Nano-scale Twins. J. Mater. Sci. Technol. 26, 289–292. https://doi.org/10.1016/S1005-0302(10)60048-5

Liu, X.C., Zhang, H.W., Lu, K., 2015. Formation of nano-laminated structure in nickel by means of surface mechanical grinding treatment. Acta Mater. 96, 24–36. https://doi.org/10.1016/j.actamat.2015.06.014

Liu, X.C., Zhang, H.W., Lu, K., 2013. Strain-Induced Ultrahard and Ultrastable Nanolaminated Structure in Nickel. Science 342, 337–340. https://doi.org/10.1126/science.1242578

Long, Q.Y., Lu, J.X., Fang, T.H., 2019. Microstructure and mechanical properties of AISI 316L steel with an inverse gradient nanostructure fabricated by electro-magnetic induction heating. Mater. Sci. Eng. A 751, 42–50. https://doi.org/10.1016/j.msea.2019.02.061

Lu, K., Lu, J., 2004. Nanostructured surface layer on metallic materials induced by surface mechanical attrition treatment. Mater. Sci. Eng. A 375–377, 38–45. https://doi.org/10.1016/j.msea.2003.10.261

Lu, X., Zhang, X., Shi, M., Roters, F., Kang, G., Raabe, D., 2019. Dislocation mechanism based size-dependent crystal plasticity modeling and simulation of gradient nano-grained copper. Int. J. Plast. 113, 52–73. https://doi.org/10.1016/j.ijplas.2018.09.007

Lu, X., Zhao, Jianfeng, Wang, Z., Gan, B., Zhao, Junwen, Kang, G., Zhang, X., 2020. Crystal plasticity finite element analysis of gradient nanostructured TWIP steel. Int. J. Plast. 130, 102703. https://doi.org/10.1016/j.ijplas.2020.102703

Maleki, E., Bagherifard, S., Unal, O., Bandini, M., Guagliano, M., 2022. On the effects of laser shock peening on fatigue behavior of V-notched AlSi10Mg manufactured by laser powder bed fusion. Int. J. Fatigue 163, 107035. https://doi.org/10.1016/j.ijfatigue.2022.107035

Rahman, K.M., Vorontsov, V.A., Dye, D., 2015. The effect of grain size on the twin initiation stress in a TWIP steel. Acta Mater. 89, 247–257. https://doi.org/10.1016/j.actamat.2015.02.008

Rai, A.K., Biswal, R., Gupta, R.K., Singh, R., Rai, S.K., Ranganathan, K., Ganesh, P., Kaul, R., Bindra, K.S., 2019. Study on the effect of multiple laser shock peening on residual stress and microstructural changes in modified 9Cr-1Mo (P91) steel. Surf. Coat. Technol. 358, 125–135. https://doi.org/10.1016/j.surfcoat.2018.11.027

Roland, T., Retraint, D., Lu, K., Lu, J., 2007. Enhanced mechanical behavior of a nanocrystallised stainless steel and its thermal stability. Mater. Sci. Eng. A 445–446, 281–288. https://doi.org/10.1016/j.msea.2006.09.041

Roland, T., Retraint, D., Lu, K., Lu, J., 2006. Fatigue life improvement through surface nanostructuring of stainless steel by means of surface mechanical attrition treatment. Scr. Mater. 54, 1949–1954. https://doi.org/10.1016/j.scriptamat.2006.01.049

Samih, Y., Beausir, B., Bolle, B., Grosdidier, T., 2013. In-depth quantitative analysis of the microstructures produced by Surface Mechanical Attrition Treatment (SMAT). Mater. Charact. 83, 129–138. https://doi.org/10.1016/j.matchar.2013.06.006

Shao, C.W., Zhang, P., Zhu, Y.K., Zhang, Z.J., Tian, Y.Z., Zhang, Z.F., 2018. Simultaneous improvement of strength and plasticity: Additional work-hardening from gradient microstructure. Acta Mater. 145, 413–428. https://doi.org/10.1016/j.actamat.2017.12.028

Sinha, S., Szpunar, J.A., Kiran Kumar, N.A.P., Gurao, N.P., 2015. Tensile deformation of 316L austenitic stainless steel using in-situ electron backscatter diffraction and crystal plasticity simulations. Mater. Sci. Eng. A 637, 48–55. https://doi.org/10.1016/j.msea.2015.04.005

Tao, N.R., Wang, Z.B., Tong, W.P., Sui, M.L., Lu, J., Lu, K., 2002. An investigation of surface nanocrystallization mechanism in Fe induced by surface mechanical attrition treatment. Acta Mater. 50, 4603–4616. https://doi.org/10.1016/S1359-6454(02)00310-5

Üçok, İ., Ando, T., J. Grant, N., 1991. Property enhancement in Type 316L stainless steel by spray forming. Mater. Sci. Eng. A 133, 284–287. https://doi.org/10.1016/0921-5093(91)90070-4

Wen, M., Liu, G., Gu, J., Guan, W., Lu, J., 2009. Dislocation evolution in titanium during surface severe plastic deformation. Appl. Surf. Sci. 255, 6097–6102. https://doi.org/10.1016/j.apsusc.2009.01.048

Williamson, G.K., Smallman, R.E., 1956. III. Dislocation densities in some annealed and cold-worked metals from measurements on the X-ray debye-scherrer spectrum. Philos. Mag. 1, 34–46. https://doi.org/10.1080/14786435608238074

Wu, X., Tao, N., Hong, Y., Lu, J., Lu, K., 2005. $\gamma \rightarrow \varepsilon$ martensite transformation and twinning deformation in fcc cobalt during surface mechanical attrition treatment. Scr. Mater. 52, 547–551. https://doi.org/10.1016/j.scriptamat.2004.12.004

Wu, Y., Guelorget, B., Sun, Z., Déturche, R., Retraint, D., 2019. Characterization of gradient properties generated by SMAT for a biomedical grade 316L stainless steel. Mater. Charact. 155, 109788. https://doi.org/10.1016/j.matchar.2019.109788

Xiong, Z., Jiang, Y., Yang, M., Zhang, Y., Lei, L., 2022. Achieving superior strength and ductility in 7075 aluminum alloy through the design of multi-gradient nanostructure by ultrasonic surface rolling and aging. J. Alloys Compd. 918, 165669. https://doi.org/10.1016/j.jallcom.2022.165669

Yuan, S., Branicio, P.S., 2020. Gradient microstructure induced shear band constraint, delocalization, and delayed failure in CuZr nanoglasses. Int. J. Plast. 134, 102845. https://doi.org/10.1016/j.ijplas.2020.102845

Zeng, Z., Li, X., Xu, D., Lu, L., Gao, H., Zhu, T., 2016. Gradient plasticity in gradient nano-grained metals. Extreme Mech. Lett. 8, 213–219. https://doi.org/10.1016/j.eml.2015.12.005

Zhang, H.W., Hei, Z.K., Liu, G., Lu, J., Lu, K., 2003. Formation of nanostructured surface layer on AISI 304 stainless steel by means of surface mechanical attrition treatment. Acta Mater. 51, 1871–1881. https://doi.org/10.1016/S1359-6454(02)00594-3

Zhang, T., Collins, D.M., Dunne, F.P.E., Shollock, B.A., 2014. Crystal plasticity and high-resolution electron backscatter diffraction analysis of full-field polycrystal Ni superalloy strains and rotations under thermal loading. Acta Mater. 80, 25–38. https://doi.org/10.1016/j.actamat.2014.07.036

Zhang, Y., Yang, C., Zhou, D., Zhe, Y., Meng, L., Zhu, X., Zhang, D., 2019. Effect of stacking fault energy on microstructural feature and back stress hardening in Cu-Al alloys subjected to surface mechanical attrition treatment. Mater. Sci. Eng. A 740–741, 235–242. https://doi.org/10.1016/j.msea.2018.10.106

Zhao, G.-H., Xu, X., Dye, D., Rivera-Díaz-del-Castillo, P.E.J., 2020. Microstructural evolution and strain-hardening in TWIP Ti alloys. Acta Mater. 183, 155–164. https://doi.org/10.1016/j.actamat.2019.11.009

Zhao, J., Lu, X., Liu, J., Bao, C., Kang, G., Zaiser, M., Zhang, X., 2021. The tension-compression behavior of gradient structured materials: A deformation-mechanism-based strain gradient plasticity model. Mech. Mater. 159, 103912. https://doi.org/10.1016/j.mechmat.2021.103912

Zhao, J., Lu, X., Yuan, F., Kan, Q., Qu, S., Kang, G., Zhang, X., 2020. Multiple mechanism based constitutive modeling of gradient nanograined material. Int. J. Plast. 125, 314–330. https://doi.org/10.1016/j.ijplas.2019.09.018

Zhao, J., Pan, X., Li, J., Huang, Z., Kan, Q., Kang, G., Zhou, L., Zhang, X., 2022. Laser shock peened Ti-6Al-4 V alloy: Experiments and modeling. Int. J. Mech. Sci. 213, 106874. https://doi.org/10.1016/j.ijmecsci.2021.106874

Zhou, J., 2018. Experimental Study and Multi-scale Modelling of LCF Behaviour of Austenitic Steels Treated by SMAT. UNIVERSITE DE TECHNOLOGIE DE TROYES.

Zhou, J., Sun, Z., Kanouté, P., Retraint, D., 2018. Reconstruction of residual stress and work hardening and their effects on the mechanical behaviour of a shot peened structure. Mech. Mater. 127, 100–111. https://doi.org/10.1016/j.mechmat.2018.09.005

Zhou, J., Sun, Z., Retraint, D., 2021. Elastic and elastic-plastic stress release due to material removal in measurement of in-depth residual stresses. Int. J. Press. Vessels Pip. 191, 104380. https://doi.org/10.1016/j.ijpvp.2021.104380

Zhu, K.Y., Vassel, A., Brisset, F., Lu, K., Lu, J., 2004. Nanostructure formation mechanism of α-titanium using SMAT. Acta Mater. 52, 4101–4110. https://doi.org/10.1016/j.actamat.2004.05.023

Zhu, L., Ruan, H., Chen, A., Guo, X., Lu, J., 2017. Microstructures-based constitutive analysis for mechanical properties of gradient-nanostructured 304 stainless steels. Acta Mater. 128, 375–390. https://doi.org/10.1016/j.actamat.2017.02.035